

Electronic Supplementary Information

Rational Design of Nanowall Photoelectrode for Efficient Solar Water Splitting

Min Zhou,^a Jian Bao,^a Minshan Tao,^a Rui Zhu,^a Yongquan Zeng,^a Zongwen Wei^b and Yi Xie^{*a}

^a Department of Nanomaterials and Nanochemistry, Hefei National Laboratory for Physical Sciences at Microscale, University of Science and Technology of China, Hefei 230026, P. R. China

^b Department of Modern Physics, University of Science and Technology of China, Hefei 230026, China

* Address correspondence to yxie@ustc.edu.cn

S1. Experimental Section.

Fabrication of Bi₂WO₆ Films. In a typical procedure, Bi (NO₃)₃·5H₂O (0.5 mmol) and Na₂WO₄·2H₂O (0.25 mmol) were respectively dissolved in ethylene glycol (25 ml) under ultrasonication for 10 min, and then the two solutions were mixed together. After magnetic stirring for another 1 min, the mixture was transferred to a Teflon-lined stainless steel autoclave and filled up to 80% of its total volume. A piece of bare tin-doped indium oxide (ITO) glass, which had been cleaned under ultrasonication by acetone, ethanol, and distilled water sequentially, was immersed vertically into the autoclave. Then the autoclave was heated to 160 °C at a ramping rate of 5 °C min⁻¹ and maintained at this temperature for 20 h. After the autoclave was cooled to room temperature, a thin layer of white-colored film was formed on the substrate. Then the glass was washed for several times with distilled water and ethanol, and dried in a vacuum drying oven at 60 °C for 6 h. For comparison, double-/triple-/quadruple-wall Bi₂WO₆ films with similar thickness were fabricated by shortening the ultrasound treatment time to 5 min, 8 min and 9 min, respectively. The single-wall film can be prepared by decreasing the ultrasound treatment time to 3 min and adding 1 g PEG 4000. The planar film was prepared by drop-coating and calcination at 300 °C for 2 h with the ramping rate of 2 °C min⁻¹. Bi (NO₃)₃·5H₂O and H₂WO₄ were dissolved in ethylene glycol as the precursor solution.

Structure and Optical Characterization. The X-ray diffraction (XRD) patterns were recorded by using a Philips XQPert Pro Super diffractometer with CuK α radiation ($\lambda=0.154178$ nm). The field emission scanning electron microscopy (FE-SEM) images were performed by using a JEOL JSM-6700F field emission scanning electron microscope (15 kV). The high-resolution transmission electron microscopy (HR-TEM) images, the corresponding selected area electron diffraction (SAED) patterns and Energy-dispersive X-ray spectroscopy (EDS) were taken on a JEOL 2010 high-resolution transmission electron microscope performed at 200 kV. Room-temperature UV-vis absorption spectra were recorded on a Perkin Elmer Lambda 950 UV/Vis-NIR spectrophotometer. The solid-state I-V measurements in the dark were measured on electrochemical station (CHI660B, Shanghai Chenhua Limited, China). Silver paste was used to make connections from the current–voltage testing system to the bottom ITO substrate and the top Bi₂WO₆ layer is in a double-probe configuration and set as voltage bias mode. The distance between the electrodes and between electrode and the edge of film were both kept the same.

Photoelectrochemical Measurement. Photoelectrochemical test systems were composed of a standard three-electrode configuration with the Bi₂WO₆ nanowall film electrode as photoanode. The nanowall films with a Pt counter electrode and an Ag/AgCl reference electrode were immersed in a degassed 0.5 mol L⁻¹ Na₂SO₄ solution, which was purged with nitrogen for 10 min prior to the measurement. The photoelectrochemical properties was measured on electrochemical station (CHI660B, Shanghai Chenhua Limited, China) in ambient conditions under illumination using a 300 W Xe lamp (PLS-SXE300/300UV, Trusttech Co., Ltd. Beijing) with a 400 nm cutoff filters, respectively. The power density of light source used in the measurement is 50 mW cm⁻². The potential was swept from 0 to +0.9 V (vs. Ag/AgCl) at a sweep rate of 10 mV s⁻¹. Incident photon-to-current efficiency (IPCE) spectra were measured on a QE/IPCE Measurement Kit (Newport, USA), while all the kit components were in control of Oriel Tracq Basic V5.0 software automatically. The light from a 300 W xenon lamp was focused through a monochromator (74125 Oriel Cornerstone 260 1/4 m) onto the cell, and the monochrometer was incremented through the spectral range (300–450 nm) to generate a photocurrent action spectrum with a sampling interval

of 10 nm and a current sampling time of 2 s, where the light intensity and the photocurrent generated were measured with a 2931-C dual channel power/current meter and a 71675 calibrated UV silicon photodetector. The measured potentials vs Ag/AgCl were converted to the reversible hydrogen electrode (RHE) scale according to the Nernst equation:

$$E_{\text{RHE}} = E_{\text{Ag/AgCl}} + 0.0591 \text{pH} + E^{\circ}_{\text{Ag/AgCl}}$$

where E_{RHE} is the potential vs RHE, $E_{\text{Ag/AgCl}}$ the measured potential against the Ag/AgCl reference electrode, and $E^{\circ}_{\text{Ag/AgCl}}$ is = 0.1976 V at 25 °C.

IPCE and APCE can be expressed concretely as follows:

$$\text{IPCE} = \eta_{e-h+} \eta_{\text{transport}} \eta_{\text{interface}} = hcI / \lambda J_{\text{light}}$$

$$\text{APCE} = \eta_{\text{transport}} \eta_{\text{interface}} = \text{IPCE} / \eta_{e-h+} = \text{IPCE} / (1 - 10^{-A})$$

Where η_{e-h+} is light harvesting efficiency (the efficiency of electron-hole (e^-/h^+) pairs generated per incident photon flux), $\eta_{\text{transport}}$ is the efficiency of charge transport, and $\eta_{\text{interface}}$ is the efficiency of interfacial charge transfer. h is Planck's constant, c is the speed of light, I is the photocurrent density ($\mu\text{A cm}^{-2}$) measured under monochromatic illumination at the wavelength of the incident light λ (nm), and J_{light} is the measured irradiance at the specific wavelength ($\mu\text{W cm}^{-2}$). A is the absorption of film at a specific wavelength.

S2. The Detailed Reasons for Choosing Bi_2WO_6 as Model Material.

For the outward embodiment strongly depends on its internal crystal structure, it is important to choose a proper material to achieve the fabrication of alternate dielectric units. As well known, layered compound may be a hopeful choice. Among the candidates, Bi_2WO_6 , as a typical Aurivillius layered oxides, possesses a sandwiched structure with alternately polar charged layers stacking along c-axis. The charges on the surfaces of this kind of material make it much easier to fabricate the alternate dielectric hierarchical structure, as attested by many previous literatures.¹⁻³ In addition, Bi_2WO_6 has attracted considerable attention due to its great potential in the utilization of solar energy.²⁻³ Hence, Bi_2WO_6 was selected as a model material to realize our conception.

S3. Corresponding characterization of multi-wall film.

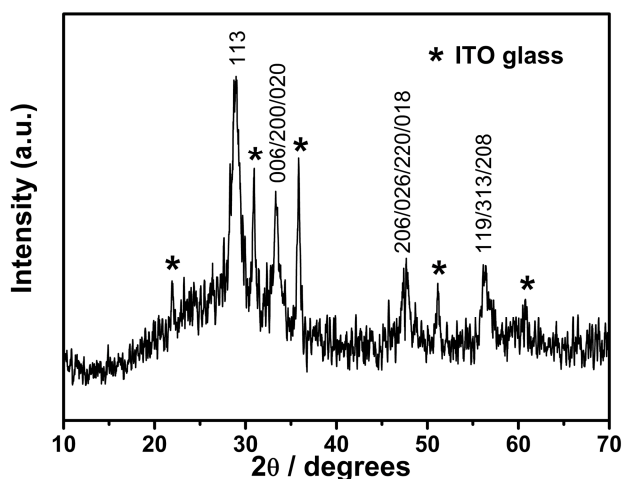


Fig. S1. The XRD pattern of Bi_2WO_6 multi-wall nanowall film, peaks generated by the ITO substrate are marked with * symbol.

Fig. S1 shows the representative XRD pattern of as-obtained thin films deposited on ITO glass. Peaks generated by the ITO substrate are marked with * symbol. All the other peaks in the diffraction pattern can be assigned to the orthorhombic Bi_2WO_6 , with the calculated lattice constant $a=5.457\text{\AA}$, $b=5.436\text{\AA}$, and $c=16.427\text{\AA}$, which are consistent with the value of JCPDS card 73-1126. No redundant peaks of any other phase are indexed, suggesting the purity of the final film.

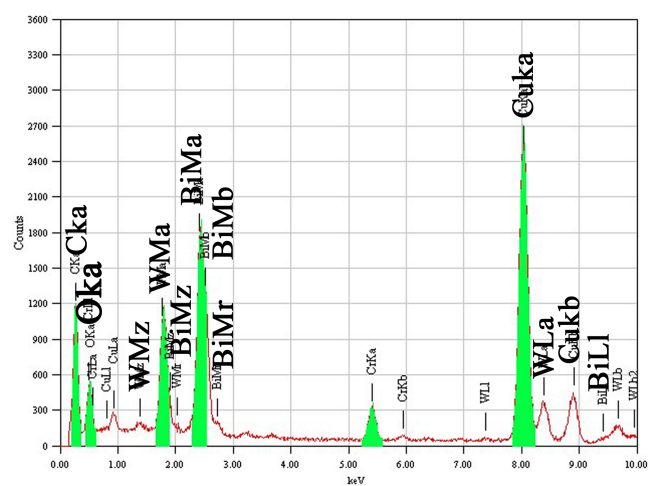


Fig. S2. The EDS spectra of the Bi_2WO_6 multi-wall nanowall film.

The EDS analysis records the elements at various locations of Fig. 1C. The analysis reveals that the film consists of bismuth, tungsten, and oxygen (copper and chromium signals arise from the TEM grid). No other elements, such as sodium or nitrogen, are detected. Furthermore, the Bi/W ratio is confirmed to be 2.1:1, in consensus with the stoichiometric ratio of Bi_2WO_6 .

S4. The growth mechanism for the oriented facets.

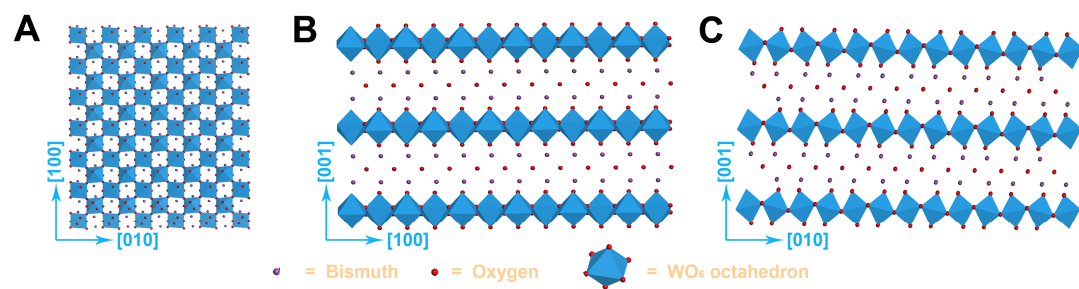


Fig. S3. Representation of orthorhombic Bi_2WO_6 structure ($6 \times 6 \times 1$ cells) along different directions (A) View along [001], (B) View along [010], (C) View along [100].

Determined by its intrinsic crystal structure, the nucleus grow anisotropically and ultimately the nanosheet is consisted of some parallel nanoflakes with (001) facet exposed. The orthorhombic

Bi_2WO_6 are built up as perovskite-like $(\text{WO}_4)_n^{2-}$ (corner-shared WO_6 octahedron) layers and alternating $(\text{Bi}_2\text{O}_2)_n^{2+}$ layers sandwiched between WO_6 octahedral layers, stacking along the c axis.⁴⁻⁶ As is well known, the morphology of the nanostructures is strongly dependent on the relative chemical potential.⁷ According to the Gibbs-Thompson theory, the relative chemical potential of crystals is simply proportional to their surface-atom ratio, which is determined by the average of dangling bonds per atom over the entire crystal.⁸ On the basis of this structure of orthorhombic Bi_2WO_6 manifested in Fig. S3, the chains of octahedral-W and BiO^+ equally existed along the [100] and [010] axes, which makes the (200) and (020) facets perpendicular to these axes have much higher chemical potential compared to other facets, such as (001). Therefore, the growth rates along [100] and [010] are higher, resulting in two-dimensional growth and the eventual formation of two-dimensional nanoflakes with (001) facet exposed.

S5. Corresponding characterization of nanowall-based films with different alternate dielectric variation.

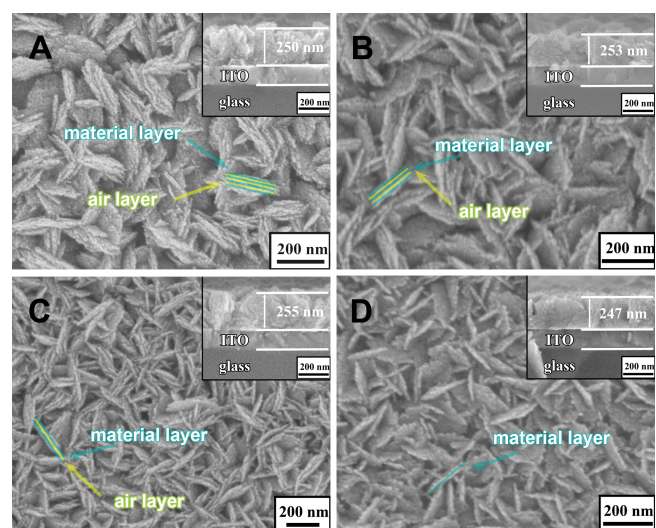


Fig. S4. Typical SEM detailed view and cross-sectional view images (insets) of the obtained alternate dielectric nanowall films with different layer number: (A) Quadruple-wall film. (B) Triple-wall film. (C) Double-wall film. (D) Single-wall film.

It should be pointed out that the nanosheets of triple-wall film are not entirely triple-wall, approximately 10 % area of which is double-wall. However, this difference has little bearing on the investigation of the trend on effects of alternate dielectric variation.

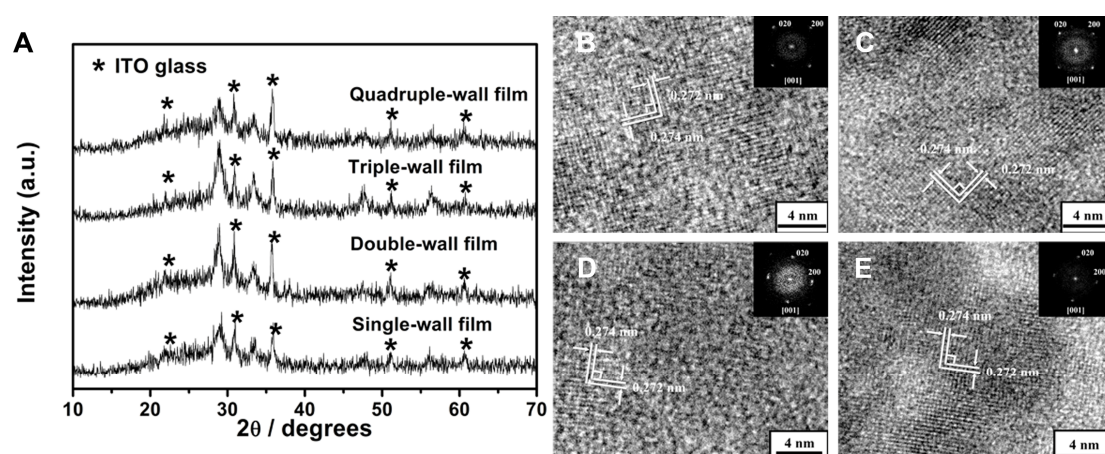


Fig. S5. (A) The XRD pattern (peaks generated by the ITO substrate are marked with * symbol) and the HRTEM images of Bi_2WO_6 film: (A) Quadruple-wall film. (B) Triple-wall film. (C) Double-wall film. (D) Single-wall film. The inset images in B-E are corresponding FFT patterns of corresponding films.

Fig. S5A shows the representative XRD patterns of nanowall films with different-layer-wall. Peaks generated by the ITO substrate are marked with * symbol. All the other peaks in the diffraction pattern can be assigned to the orthorhombic Bi_2WO_6 (JCPDS card 73-1126). No redundant peaks of any other phase are indexed, suggesting the purity of the final film. Fig. S5B-S5E show the HRTEM images of four films with inset of its corresponding fast Fourier transform (FFT) pattern. The lattice spacing of 0.274 and 0.272 nm between adjacent lattice planes corresponds to the distance of adjacent (200) and (020) crystal planes of Bi_2WO_6 , respectively. The acute angle between these two planes is 90° . The FFT pattern is indexed as orthorhombic Bi_2WO_6 along the [001] zone axis as well.

S6. Light absorption of nanowall-based films with alternate dielectric component.

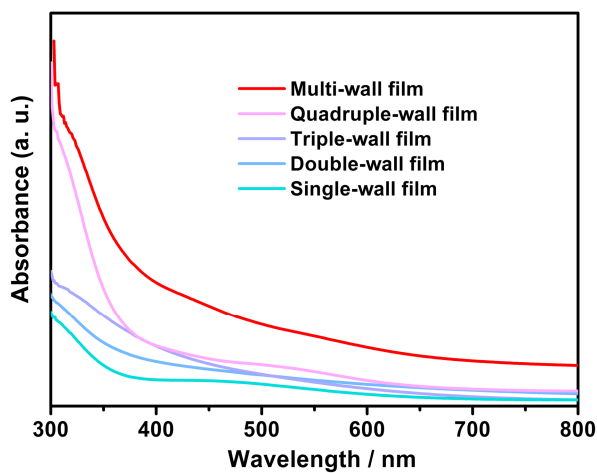
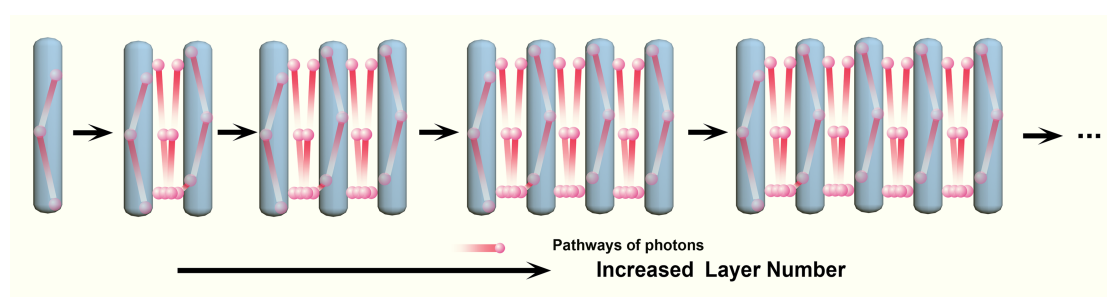


Fig. S6. Light absorption spectra of the nanowall based films with different layer number.



Scheme S1. Exaggerated diagram for the estimated path of incident photons within an aligned nanosheet

S7. Corresponding characterization of planar film.

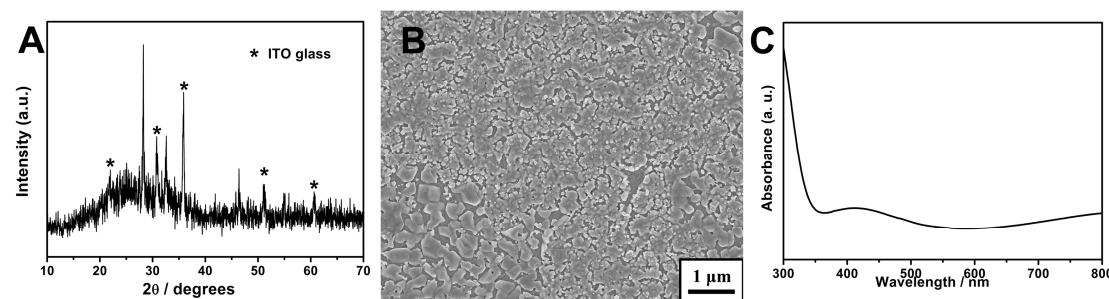


Fig. S7. (A) The XRD pattern of Bi_2WO_6 planar films, peaks generated by the ITO substrate are marked with * symbol. (B) Typical SEM overall view image of the planar films. (C) Light absorption spectra of planar films.

Fig. S7A shows the representative XRD patterns of planar film deposited on ITO glass. Peaks generated by the ITO substrate are marked with * symbol. All the other peaks in the diffraction pattern can be assigned to the orthorhombic Bi_2WO_6 , with the calculated lattice constant $a=5.457\text{\AA}$, $b=5.436\text{\AA}$, and $c=16.427\text{\AA}$, which are consistent with the value of JCPDS card 73-1126. No redundant peaks of any other phase are indexed, suggesting the purity of the final film. Typical SEM overall view of the planar film is shown in Fig. S7B. This whole film consists of assembled nanobeads with diameters of 200 - 500 nm and is full of pores with a diameter of ~100 nm. Fig. S7C is the corresponding light absorption spectra of the planar films.

S8. Relative IPCE of all the nanowall-based films and planar film.

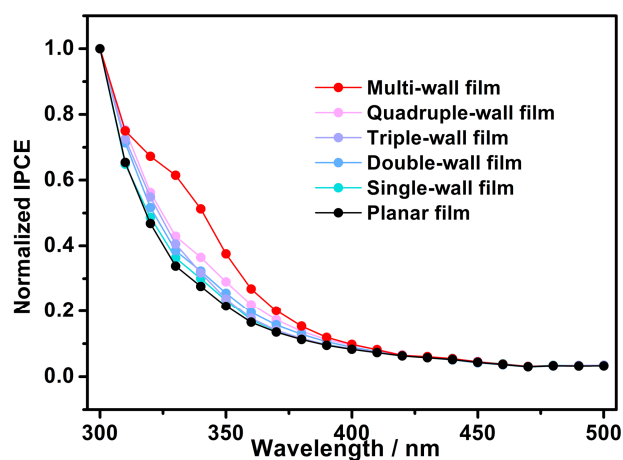


Fig. S8. Relative IPCE of all the nanowall based films and planar film normalized at a wavelength of 300 nm.

S9. Detailed photoelectrochemical performance of nanowall-based film and planar film.

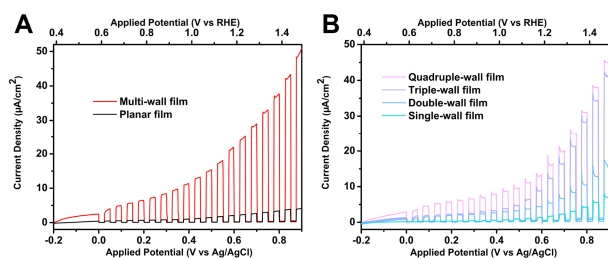


Fig. S9. Photocurrent density-potential curves of multi-wall nanowall film/planar film (A) and nanowall films with different layer number (B) as photoelectrodes upon chopped irradiation measured under visible light illumination ($\lambda > 400$ nm).

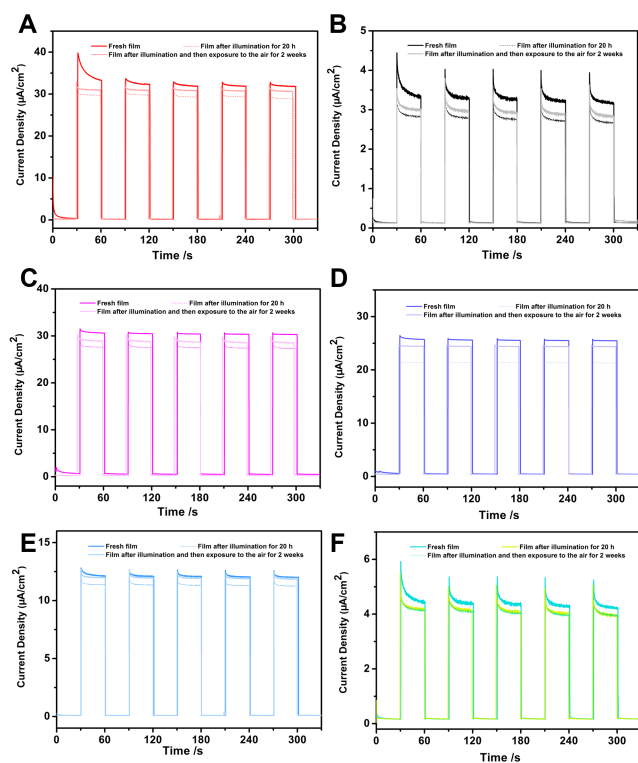


Fig. S10. Photocurrent–time dependence under visible light irradiation upon chopped irradiation of nanowall films with different layer number as photoanodes at 0.8 V vs Ag/AgCl with a sweep rate of 10 mV s^{-1} : (A) Multi-wall film. (B) Planar film. (C) Quadruple-wall film. (D) Triple-wall film. (E) Double-wall film. (F) Single-wall film. The films were measured as fresh (dark-colored lines), after illumination for 20 h (dotted lines), or after illumination and then exposure to the air for 2 weeks (light-colored lines), respectively (0.8 V vs. Ag/AgCl, a sweep rate: 10 mV s^{-1}).

Notes and references

1. A. Kudo, S. Hijii, *Chem. Lett.* 1999, 1103.
2. L. Zhang, W. Wang, L. Zhou, H. Xu, *Small* 2007, **3**, 1618.
3. F. Amano, K. Nogami, B. Ohtani, *J. Phys. Chem. C* 2009, **113**, 1536.
4. J. Tang, Z. Zou, J. Ye, *Cat. Lett.* 2004, **92**, 53.
5. C. Zhang, Y. Zhu, *Chem. Mater.* 2005, **17**, 3537.
6. N. Kim, R.-N. Vannier, C. P. Grey, *Chem. Mater.* 2005, **17**, 1952.
7. Z. A. Peng, X. Peng, *J. Am. Chem. Soc.* 2002, **124**, 3343.
8. S. H. Yu, B. Liu, M. S. Mo, J. H. Huang, X. M. Liu, Y. T. Qian, *Adv. Funct. Mater.* 2003, **13**, 639.